Helical superstructures between amyloid and collagen VI in heart-derived fibrils from a patient with Light Chain Amyloidosis.

Stefano Ricagno (stefano.ricagno@unimi.it)
University of Milan https://orcid.org/0000-0001-6678-5873

Tim Schulte

Antonio Chaves-Sanjuan
University of Milano https://orcid.org/0000-0003-3287-9024

Valentina Speranzini
Department of Biosciences, Università degli Studi di Milano

Kevin Sicking
University Medical Center Göttingen, Institute for Neuropathology

Giulia Mazzini
Fondazione IRCCS Policlinico San Matteo and University of Pavia https://orcid.org/0000-0001-7695-2938

Paola Rognoni
Foundation IRCCS Policlinico San Matteo https://orcid.org/0000-0001-6350-1919

Serena Caminito
University of Pavia

Paolo Milani
Amyloidosis Treatment and Research Center, Fondazione IRCCS Policlinico San Matteo, Università Degli Studi di Pavia

Chiara Marabelli
Department of Biosciences, Università degli Studi di Milano

Alessandro Corbelli
Mario Negri Institute for Pharmacological Research

Luisa Diomede
Istituto di Ricerche Farmacologiche Mario Negri IRCCS https://orcid.org/0000-0002-2258-0531

Fabio Fiordaliso
Mario Negri Institute for Pharmacological Research

Luigi Anastasia
Università Vita-Salute San Raffaele https://orcid.org/0000-0002-0712-2161

Carlo Pappone
Università Vita-Salute San Raffaele https://orcid.org/0000-0002-0901-6135

Giampaolo merlini
Department of Molecular Medicine, University of Pavia, Pavia, Italy https://orcid.org/0000-0001-7680-3254
Martino Bolognesi
University of Milano https://orcid.org/0000-0002-9253-5170
Mario Nuvolone
Department of Molecular Medicine, University of Pavia https://orcid.org/0000-0001-8334-1684
Ruben Fernandez-Busnadiego
University Medical Center Goettingen https://orcid.org/0000-0002-8366-7622
Giovanni Palladini
University of Pavia

Article

Keywords:

Posted Date: November 21st, 2023

DOI: https://doi.org/10.21203/rs.3.rs-3625869/v1

Additional Declarations: There is **NO** Competing Interest.

Helical superstructures between amyloid and collagen VI in heart-derived fibrils from a patient with Light Chain Amyloidosis.

Tim Schulte[1]*, Antonio Chaves-Sanjuan[2]*, Valentina Speranzini[2]*, Kevin Sicking[3,4], Giulia Mazzini[5], Paola Rognoni[5], Serena Caminito[5], Paolo Milani[5], Chiara Marabelli[2], Alessandro Corbelli[6], Luisa Diomede[6], Fabio Fiordaliso[6], Luigi Anastasia[1,7], Carlo Pappone[1,7,8], Giampaolo Merlini[5], Martino Bolognesi[2], Mario Nuvolone[5], Rubén Fernández-Busnadiego[3,4,9,10], Giovanni Palladini[5], Stefano Ricagno[1,2,&]

* Authors contributed equally.

[1] Institute of Molecular and Translational Cardiology, IRCCS Policlinico San Donato, Piazza Malan 2, 20097, San Donato Milanese, Italy;

[2] Department of Biosciences, Università degli Studi di Milano, Milan 20133, Italy;

[3] University Medical Center Göttingen, Institute for Neuropathology, Göttingen, 37077 Germany

[4] Aligning Science Across Parkinson's (ASAP) Collaborative Research Network, Chevy Chase, MD, USA

[5] Amyloidosis Treatment and Research Center, Fondazione IRCCS Policlinico San Matteo, Università Degli Studi di Pavia, Pavia, 27100, Italy'

[6] Department of Molecular Biochemistry and Pharmacology, Istituto di Ricerche Farmacologiche Mario Negri IRCCS, Via M. Negri 2, Milano, 20156, Italy;

[7] Faculty of Medicine and Surgery, Vita-Salute San Raffaele University, Milan, 20132, Italy;

[8] Arrhythmia and Electrophysiology Department, IRCCS Policlinico San Donato, San Donato, Milan, 20097, Italy

[9] Cluster of Excellence "Multiscale Bioimaging: from Molecular Machines to Networks of Excitable Cells" (MBExC), University of Göttingen, Göttingen, 37077, Germany

[10] Faculty of Physics, University of Göttingen, Göttingen, 37077, Germany

& To whom correspondence may be addressed: stefano.ricagno@unimi.it , Tel. +39 02 5031 4914, Via Celoria 26, 20133, Milano (Mi), Italy

Göttingen, 37077, Germany

Abstract

Systemic light chain (LC) amyloidosis (AL) is a disease where organs are damaged by an overload of a misfolded patient-specific antibody-derived LC, secreted by an abnormal B cell clone. The high LC concentration in the blood leads to amyloid deposition at organ sites. Indeed, cryogenic electron microscopy (cryo-EM) has revealed unique amyloid folds for heart-derived fibrils taken from different patients. Here, we present the cryo-EM structure of heart-derived AL amyloid (AL59) from another patient with severe cardiac involvement. Its structure displays a stable core and two flexible segments adopting alternative conformations. Two confirmations are sterically incompatible and typically distributed on separate fibrils. Noteworthy, the fibril core harbours an extended constant domain fragment, thus ruling out the variable domain as sole amyloid building block. Surprisingly, the fibrils were abundantly concatenated with a proteinaceous polymer, here identified as collagen VI (COLVI) by immuno-electron microscopy (IEM) and mass-spectrometry. Cryogenic electron tomography (cryo-ET) showed how COLVI wraps around the amyloid forming a helical superstructure, likely stabilizing and protecting the fibrils from clearance. Thus, here we report the first structural evidence of interactions between amyloid and collagen, potentially signifying a novel pathophysiological mechanism of amyloid deposits.

Introduction

Systemic AL amyloidosis is caused by a rare plasma cell dyscrasia with an annual incidence of about 12-15 new cases per million people [1]. AL amyloidosis is due to the overexpression of an amyloidogenic LC that misfolds and forms amyloid deposits in several organs [2]. The circulating LC molecules exert proteotoxicity which concurs with the mass effect produced by amyloid deposits to fatal organ dysfunction [1]. Due to genomic recombination and somatic mutations every AL patient bears a virtually unique amyloidogenic LC sequence, originating from either the λ- or κ-gene locus [3,4]. Most patients are affected by deposits in multiple organs, but heart manifestation dictates the prognosis in ~75% of cases [5–9]. Without its associated heavy chain, free LCs fold into homodimers where each monomer consists of an N-terminal variable domain (V_L) and a C-terminal constant domain (C_L) connected by a flexible joining region [10–13]. While free LCs are eliminated rapidly under healthy conditions, abnormal levels of an amyloidogenic LC cause vast accumulations of cross-β amyloid fibrils in AL amyloidosis [1,14]. Cryo-EM has emerged as a powerful method to determine molecular structures of *ex vivo* amyloids, retrieved from patients affected by various amyloidoses [15–21]. The structures of fibrils from cardiac tissue of four AL patients, denoted as λ6-AL55, λ3-FOR005, λ1-FOR001 and λ1-FOR006, display distinct folds [3,15–19]. So far, only residues belonging to V_L were found in the structured core of the AL amyloid, resulting in high sequence variability in the core of the deposited fibrils [3,15–19]. Structures of sequence-identical amyloid from the heart and kidney of the same patient are well superposable, indicating a crucial role of the V_L sequence in determining the fibrillar structure [19]. Other sources of variability in this disease are post-translational modifications (PTM), and in particular proteolytic processing and N-glycosylation hotspots. The latter were shown to correlate with AL onset for κ LCs [22–24]. To date, glycosylation in λ LCs is not considered

a risk factor for AL [24,25], but the cryo-EM structure of λ1-FOR001 shows a covalently linked glycan that may impact the resulting amyloid fold [18].

Ancillary proteins are reproducibly found in amyloid deposits, including heparan sulphate proteoglycan, serum amyloid P-component and various extracellular matrix elements (ECM) such as collagen [1,26–30]. The ECM provides structural support for organs and tissues and is dynamically remodelled, controlling tissue homeostasis and modulating immune cell responses [31–33]. As most prominent ECM component, collagens are frequently detected in deposits extracted from different amyloidosis types [27]. Co-purified collagens seem to affect directly amyloid formation and disease progression [27,34–39]. Collagens facilitate misfolding of native human β_2-microglobulin (β2m) into amyloid, leading to fibril deposition in the joints of hemodialysis patients [36–39]. Increased collagen content was found in cerebral microvessels of patients with Alzheimer's disease, and a neuron-protective role was put forward for COLVI [40–42]. Recent evidence suggests that binding of collagens in general, but particularly COLI and COLIV, protects AL amyloid against phagocytic clearance in experimental mouse models [34,35]. Thus, collagen/amyloid interactions modulate the progression of various amyloidoses.

Here we report 4.0 and 4.1 Å resolution cryo-EM structures of N-glycosylated AL amyloid, which was extracted from the heart of a patient with cardiac AL amyloidosis and is referred to as AL59. The structures display a stable core and two flexible segments adopting alternative conformations. AL59 is the first AL amyloid structure reported to harbour an extended constant domain fragment in its core. The fold is related to that of a previously reported AL amyloid structure, belonging to the same λ3-gene subfamily. *Ex vivo* AL59 fibrils display the unique ability to interact with a polymer from the extracellular matrix, which was identified as COLVI. While COLVI was not resolved in the helical reconstruction of the amyloid, we applied IEM and cryo-ET to reveal that

COLVI wraps helically around the fibril, potentially stabilising and protecting AL59 amyloids from macrophage recognition.

Results & Discussion

Ex vivo AL59 amyloids form abundant complexes with co-purified unknown polymer

AL59 amyloids were extracted from the heart apex tissue of a 56 years old patient, who had died from progressive heart failure and systemic AL amyloidosis (Supplementary Fig. 1 and Supplementary Tab. 1). The amyloid extraction procedure is standardized in our laboratory as previously described [16,28,43]. AL59 belongs to the λ3 light chain family, and is more specifically encoded by the variable gene IGLV3-01, and IGLJ2*01 for the joining segment. Liquid chromatography tandem mass spectrometry (LC-MS/MS) carried out on extracted fibrils revealed peptide fragments corresponding to residue numbers 1-204 of AL59 (Supplementary Fig. 1). To determine the molecular structure of AL59 amyloids, cryo-EM data were collected. Inspection of raw cryo-EM micrographs of the vitrified amyloid extract revealed fibrils with an alternating width pattern, from which we estimated a crossover length of ~1,200 Å (Fig. 1a). Surprisingly, an additional polymer distinct from amyloid was abundantly present in all fibril samples extracted from AL59 cardiac tissue (Fig. 1a). This polymer was present both in isolated form and also AL59-associated. In its unbound form, the polymer exhibits a bipartite repeating structure comprising 500 Å long beads connected by 600 Å long and 50 Å thin fibres, thus exhibiting a periodicity of 1,100 Å (Fig. 1a). With further micrograph inspection, we also recognized the same bead-like shape as part of the amyloid-decorating polymer (Fig. 1a). Among 184 micrographs with higher visual contrast, we found the polymer decorating about 80% of amyloid fibrils. To unveil the structural properties of this unique

AL59/polymer complex, we also collected cryo-ET data. In agreement with the cryo-EM micrographs, tomograms revealed undecorated amyloid, free polymer, as well as abundant polymer-decorated amyloid (Fig. 1b).

The structure of glycosylated AL59 displays a stable core and two flexible segments adopting alternative conformations

To determine the structure of AL59, free and polymer-decorated amyloids were picked as single population for standard helical reconstruction [44,45]. A reference-free 2D class average of segments extracted with a box size of ~1,600 Å confirmed the estimated crossover length of ~1,200 Å (Supplementary Fig. 2a). Class averages of shorter segments, extracted with a box size of 302 Å, revealed the amyloid-characteristic β-spine (Supplementary Fig. 2b). The 2D class averages were characteristic of amyloid, lacking any features attributable to the abundant polymer. From the initially extracted ~121 k segments, ~16 k, ~22 k and ~27 k segments were assigned to three distinct 3D classes, named 'bent', 'straight' and 'mixed' (Fig. 2a). The fourth class comprising ~56k particles lacked clear structural features and was named 'blurry' (not shown).

Cross-sections through the structured classes revealed variations of a shared fold (Fig. 2a and 2b), comprising a meandering double layer with three sharp kinks (i-iii). While the central segment appears virtually identical in all classes, the terminal and β-arc segments adopt different conformations due to altered kink angles. The bent and straight classes take angles of 105° and 120° at the first kink, respectively, as well as 90° and 125° at the third kink. The bent and straight classes were reconstructed to resolutions of 4.1 and 4.0 Å, respectively (Supplementary Tab. 2). The reconstruction of the mixed class was limited to a maximum resolution of 5.2 Å. Its cross-section shows β-arc and terminal

147 segment conformations as observed for the bent and straight structures, respectively. As
148 this class features kink angles of both other structures, we did not build a molecular
149 model into its lower resolution map.

150 The structure of the straight class was built manually starting from the disulphide bond
151 between residue Cys-22 and Cys-87, observed clearly in both maps at identical position
152 (Fig. 2c). The single proto-filament comprises residues 1-119, 71 of which form 12 β-
153 strands (Fig. 2d). The three kinks of the meandering double-layer are marked with residue
154 pairs Pro-14/Phe-97, Pro-39/Asp-81 and Pro-54/Ala-70 (Fig. 2c). Compared to the
155 straight structure, the bent model lacks four and eight residues at the N- and C-*termini*,
156 respectively, as well as five residues between Phe-97 and Leu-103 (Fig. 2c and 2d). The
157 C-terminal tail fragment in the bent structure was modelled, but we are uncertain about its
158 identity due to non-contiguous density (Fig. 2c). The missing segments may be flexible or
159 absent due to proteolysis. Superimposed maps highlight the virtually identical central
160 part, and altered conformations of the terminal and β-arc segments (Fig. 3a). A high
161 number of Gly and Pro residues renders AL59 prone to adopt alternative conformations,
162 despite considerable number of interactions stabilizing the fibril core (Supplementary Fig.
163 3). In the straight structure, β-arc residue Gly-63 contacts Gly-98-Gly-100, but this
164 contact is not stabilized (Supplementary Fig. 3). The new position of the β-arc in the bent
165 structure is stabilized by weak polar interactions between the side-chains of Ser-64 and of
166 Thr-93, as well as the backbone of Asp-91 (Supplementary Fig. 3a). The opposing N- and
167 C-terminal tails are kept close by hydrophobic interactions in the straight structure, while
168 in the bent structure they are more loosely associated (Supplementary Fig. 3).

169 Both straight and bent AL59 structures stack rather flat within fibrils, exhibiting maximal
170 Cα height differences of 7.6 and 7.9 Å, respectively (Fig. 2e). Noteworthy, if stacked on

171 the same fibril, the terminal segments of the bent and straight structures would clash (Fig.
172 3a), suggesting that the two classes are unlikely to coexist within one fibril. Thus, we
173 analysed the distribution of the three classes among individual fibrils: indeed, the bent
174 class was more likely to be found on distinct fibrils, and separated from the straight and
175 the mixed classes (Fig. 3b and Supplementary Fig. 4). In fibrils containing segments of
176 more than one type, long consecutive regions of the same class are interspersed by short
177 regions of the other classes, especially of the blurry class (Fig. 3b, Supplementary Fig. 4).
178 This analysis suggests that the bent class is typically found alone or in association with
179 the blurry class. The straight class tends to cluster but seems also compatible with the
180 mixed class. The observed distribution differs from the previously reported combined
181 stacking of conformers in λ3-FOR005 amyloid fibrils [15].

182 Finally, an additional density around Asn-19 was modelled as N-linked N-acetyl
183 glucosamine (NAG) in both structures, as glycosylation was also detected by mass
184 spectrometry, 2D-PAGE and western blot (Fig. 2c, Supplementary Fig. 1). N-
185 glycosylation has been reported to correlate with amyloidogenic κ, but not λ LCs [24,46].
186 Curiously, among the five *ex vivo* LC amyloid structures [3,15–19], AL59 is the second with a
187 structurally confirmed glycosylation site, indicating that glycosylation of λ-LCs may be
188 more common than expected.

189 In summary, the structures of glycosylated AL59 display a stable core and two flexible
190 segments adopting alternative conformations. The observed alternative conformations of
191 the terminal segment are sterically incompatible, possibly explaining their separation on
192 distinct fibrils.

193

AL59 ***adopts a fold related to λ3-FOR005, but harbours an extended constant domain fragment in its amyloid core***

In keeping with the four other reported *ex vivo* LC amyloid structures (Fig. 4a) [3,15–19], AL59 adopts a fold substantially different from its native structure (Fig. 4b), but retains the conserved disulphide bond between Cys-22 and Cys-87. The 59-64% sequence-identical V_L-domains of the λ1- and λ6-subfamily members (Fig. 4a) adopt amyloid folds different from AL59. Interestingly, the structure of the ~70% sequence-identical and non-glycosylated λ3-FOR005 is superimposable on AL59 with a root mean square deviation of ~4 Å over 81 aligned residues (Fig. 4a and c). The two related folds exhibit similar positioning of the disulphide bond and CDR segments (Fig. 4c). Glycosylation does not seem to impact this specific amyloid fold. In contrast, the authors of a previous study suggested that glycosylation of λ1-FOR001 contributes to define its specific amyloid fold [18]. Thus, here we show that two LCs belonging to the same germline subfamily, but from different individuals, adopt a related amyloid fold. This observation corroborates our previous findings of identical structure of fibrils extracted from different organs of the same individual, indicating that the fibril fold is dictated by its primary sequence [19].

In contrast to the previously reported LC amyloid structures [3,15–19], AL59 is the first structure with a C_L domain fragment extending beyond residue position 106, that is located within the V_L-C_L joining region. A model for LC amyloid aggregation posits that proteolytic cleavage of the joining region is required to trigger fibrils formation by the amyloidogenic V_L domain molecules [47,48]. Evidently, such a model cannot be applied to AL59 amyloid aggregation. If a proteolytic event is necessary to destabilise AL59 native fold, it may occur in the C_L domain. Furthermore, we applied our established LC-MS/MS protocol which revealed proteolysis hotspots in the C_L domain of AL59 (Fig. 4b),

similarly to those reported for λ6-AL55 and λ1-H7 [28,43]. These observations support our previous interpretation that *in vivo* proteolysis occurs mostly *post* aggregation [28,43].

Thus, λ3-AL59 amyloid adopts a fold related to LC fibrils derived from the same germline subfamily, regardless of originating from a different patient. The inclusion of an extended C_L-derived fragment in the AL59 amyloid core, combined with the extensive fragmentation of the C_L domain, point at the C_L domain as main target for *in vivo* proteolysis.

Collagen VI is co-extracted with AL59 fibrils from cardiac tissue

To facilitate identification of the additional polymer observed in the micrographs, 2,208 beads (Fig. 1a) were picked manually for single-particle analysis (SPA). 2D class averages of the beads revealed two half-beads, each ~140 Å wide and ~165 Å long, connected by a ~20 Å wide and ~90 Å long intra-bead fibre (Fig. 5a). The two half-beads adopt non-identical orientations, rotated around the intra-bead fibre. Each half-bead exhibits a tripartite structure with a head, an intermediate central body, and two tails lining the intra-bead fibre (Fig. 5a). Inter-bead fibres were apparent, but not well resolved. Our search for a polymer with matching structure was facilitated by LC-MS/MS identification of collagen VI (COLVI) subunits α1, α2 and α3 as major components in the AL59 extract (Supplementary Tab. 3). The structural organization of the abundant polymer was matched visually to the previously described unique architecture of COLVI bead-on-a-string microfibrils [49–54]. In line with the posited COLVI assembly model (Fig. 5b), integrated from biochemical and structural results collected over decades [49–53,55,56], the two half-beads appear two-fold symmetric in reference-free 2D class averages (Fig. 5a). Focused heterogeneous 3D refinement of C2 symmetry-expanded half-beads yielded

a 13 Å resolution map (Fig. 5c and Supplementary Fig. 5 and 6), resembling the available 48 Å resolution map of COLVI extracted from bovine cornea [51]. As predicted by the assembly model, additional two-fold symmetry splits the half-beads into quarter-beads. While enforced symmetry improved the FSC-based resolution estimate to 12 Å, map interpretability was not markedly improved. We did not construct a molecular model, but found ample space to place 11 VWFA domains in the quarter-bead volume (Supplementary Fig. 6b). Three additional domains may be placed in less defined parts of the map. The intra- and inter-bead fibre volumes can accommodate four collagen triple helices placed next to each other, with a width that is probably larger than the predicted nanoscale rope architecture [57–60].

In summary, our single particle cryo-EM and LC-MS/MS data allowed us to identify the co-purified abundant polymer in the AL59 amyloid extract as COLVI.

COLVI forms helical superstructures with AL59 fibrils

To unambiguously identify COLVI as the AL59-decorating polymer, we performed IEM applying a COLVI-specific [61] polyclonal antibody followed by gold-conjugated secondary antibody staining of the same extract used for cryo-EM and cryo-ET sample preparations. The IEM images revealed single amyloid fibrils, amyloid clusters and free COLVI polymers tagged by gold (Fig. 6a and Supplementary Fig. 7). Gold particles were located within distances of ~150 Å to single AL59 fibrils, corresponding to half the theoretical length of two coupled antibodies, thus marking complexes between AL59 and COLVI and identifying COLVI beads. Gold duplets with centre-to-centre distances of ~240 Å possibly mark two distinct quarters within the same full-bead of COLVI. When

the same sample was treated only with gold-conjugated secondary antibody, no gold particles were found (Fig. 6a and Supplementary Fig. 8).

COLVI was not observed in the helical reconstruction of AL59, likely due to the helical symmetry applied during the reconstruction procedure. The repeat distance of the amyloid building block is ~5 Å, while this value is 1,100 Å for COLVI-beads. Indeed, applying SPA we obtained a single 2D class average from 78 non-duplicated particles, which we interpreted as amyloid with associated COLVI-bead (Fig. 5d). A speculative arrangement of the AL59 fibril and COLVI-bead provides visual support for our interpretation (Fig. 5d).

To better characterize the architecture of unique AL59/COLVI complexes, we applied cryo-ET (Fig. 1b and 6b). In the reconstructed tomograms, the majority of AL59 was decorated by COLVI (Fig. 6b). Generally, the rigid AL59 fibrils were better defined than the heterogeneous COLVI decorating density. Thus, although we observed bead-like structures in amyloid-associated COLVI (Fig. 1b), our attempts to average sub-tomograms were not successful, preventing a molecular reconstruction of the AL59-COLVI complex. Notably, COLVI wraps around the central AL59 fibril, adopting the helical twist and rise values of the amyloid but with a three times larger helical radius (Fig. 6b). While COLVI adopts a non-helical superstructure on its own, the amyloid fibril imprints its helical structure on COLVI, resulting in complexes with an interaction interface spanning for thousands of angstrom. Such a chirality transfer is regarded as fundamental mechanism across scales in natural and artificial systems [62–65]. Specifically amyloids, exploited in nanotechnology and biotechnology, were reported as chirality inducers [63,66,67].

Recently, collagen was reported to play a protective role against amyloid clearance by macrophages [34,35]. The helical superstructures between AL59 and COLVI with such extensive interaction surfaces can exemplify how collagen may contribute to amyloid stabilisation and may hide misfolded aggregates from macrophage activity [34,35]. Earlier studies have also demonstrated adverse effects of collagen in various other amyloidoses. In dialysis-related Aβ2M amyloidosis, collagen facilitates β2m aggregation and interacts weakly with mature β2m fibrils [36–39]. In ATTR amyloidosis, transthyretin (TTR) tends to aggregate in the presence of basement membrane components such as collagen IV, whose expression correlates with amyloid accumulation [68,69]. Collagen levels are also increased in the brains of Alzheimer's patients where collagen seems to play a neuroprotective role and facilitates the formation of mature Aβ fibrils [40–42,70]. Then why had no structural evidence of such interactions been reported to date? A possible answer is that these interactions are typically weak and do not withstand the forces exerted during extraction. The unexpected abundance of COLVI in our micrographs may be related to unique amyloid features. LC fibrils in different AL patients present distinct surface residues, thus forming intermolecular complexes with variable stability. By serendipity, AL59 amyloids can interact strongly with COLVI, resulting in the abundant and reproducible observation of the AL59/COLVI complex in our *ex vivo* extracts. Moreover mild extraction protocols may facilitate the observation of such complexes. Remarkably, a micrograph of λ3-FOR005, shown in Supplementary Fig. 1 of that study [15], displays an amyloid-concatenated polymer resembling COLVI. Thus, the concatenation of amyloid with collagen, exemplified here as helical superstructures, may represent a general mechanism by which collagen(s) could modify the recognition of amyloid by host defence mechanisms.

In summary, here we report the cryo-EM structure of AL59 amyloids extracted from an AL patient with severe cardiac involvement. Glycosylated λ3-AL59 adopts two main structures with a common fold: they are sterically incompatible and are found on different fibrils, suggesting two independent aggregation events for fibrils harbouring bent or straight fibrils. Surprisingly, AL59 fibrils form helical superstructures with COLVI, representing the first evidence of a stable interaction between amyloid and ECM components. This observation provides insights about the potential role of collagen as a modulating agent of amyloid deposits, potentially signifying a novel pathophysiological mechanism for amyloidoses.

Materials & Methods

Extraction and characterization of amyloid deposits from the heart of patient AL59

Clinical characteristics of patient AL59. Fibrils were derived from autoptic heart tissue (apex) of patient AL59 affected by AL amyloidosis with cardiac involvement and died of progressive heart failure. After autopsy examination, showing Congo red positivity in heart, tissue was stored frozen (−80 °C) without fixation until use. AL amyloidosis had been diagnosed 10 months earlier on abdominal fat aspirate, where amyloid deposits were evaluated by Congo red staining under polarized light and amyloid typing was confirmed by immuno-electron microscopy [71]. Organ involvement was defined according to international criteria [72]. Baseline clinical and demographic information are listed in Supplementary Tab. 1. The patient was treated with cyclophosphamide, bortezomib and dexamethasone. After four cycles, hematologic partial response was reached (dFLC levels declined from 280 to 111 mg/L), with cardiac progression (NT-proBNP levels rose from 6,043 to 17,600 ng/L). Treatment was subsequently stopped for progressive heart failure. This study was approved by the Ethical Committee of Fondazione IRCCS Policlinico San Matteo and was performed in accordance with the Declaration of Helsinki.

cDNA sequencing of monoclonal LC (Pavia). Total RNA was extracted from 10^7 bone marrow mononuclear cells using TRIzol reagent (Life Technologies, Paisley, United Kingdom). Nucleotide sequence of monoclonal LC variable region (V_L) was cloned by a universal inverse-PCR strategy that preserves its original sequence at 5' and 3' ends [73]. Briefly, primers specific for the 5' (λ-C_{LA}: 5'-AGTGTGGCCTTGTTGGCTTG-3') and 3' (λ-C_{LB}: 5'-GTCACGCATGAAGGGAGCAC-3') ends of the λ-LC C_L were used. The PCR fragment was ligated into a cloning vector and amplified. After plasmid purification, insert was sequenced to deduce the V_L chain sequence. To determine the germline of

AL59-V_L, the sequence was aligned to the EMBL-GenBank, V-BASE (V BASE Sequence Directory, MRC Centre for Protein Engineering, Cambridge, UK) and IMGT sequence directories. The sequence showed the highest homology with the *IGLV3-1* and *IGLJ2*0* germline gene. The AL59-V_L sequence was deposited in the GenBank database (GenBank OR567864).

Fibril purification from heart tissues of patient AL59. Fibrils were extracted from 500 mg of heart tissue (apex) as previously described [16], obtaining six consecutive water-extracted fractions of 750 μl each. To evaluate the yield, 50 μl of each fraction were vacuum dried and re-suspended in 20 μl of 8 M urea to solubilize the fibrils. After protein quantification, using microBCA assay (Thermo Fisher Scientific), fibril patterns were analyzed by SDS-PAGE under denaturing and reducing conditions. Water extract fraction #3 was selected for proteomic and cryo-EM analyses.

N-glycosylation proteomic analyses by PNGase F digestion. For western blot and LC-MS/MS analyses protein was deglycosylated using PNGase F (New England Biolabs) under denaturing and non-denaturing (glycerol-free) conditions, respectively [24].

Proteomic characterization of enriched amyloid fibrils derived from heart tissues of patient AL59. About 250 mg of heart tissue (apex) were used for the fibril enrichment procedure, performed on ice and in presence of protease inhibitors. The obtained pellet was characterized for LC fragments as described previously [28,43]. Briefly, 2D-polyacrylamide gel electrophoresis was performed under denaturing and reducing conditions. Proteins were detected using GelCode™ Blue Stain Reagent (Pierce). Subsequently, glycoproteins were revealed on the same gel as magenta spots applying the Glycoprotein Staining Kit (Pierce) according to manufacturer's instructions. LCs were identified by western blot, using polyclonal rabbit anti-human λ LC antibody (1:25,000,

A0914, Dako). To identify the N- and C-"terminomes" of LC proteo-forms in the amyloid fibrils [24,28], bottom-up proteomic analysis was performed on proteins chemically derivatized at the N- and C-*termini* by dimethyl labeling and amidation with ethanolamine, respectively.

Liquid chromatography – tandem mass spectrometry (LC-MS/MS) analysis and database search. LC-MS/MS analyses were performed on a Dionex Ultimate 3000 nano-UHPLC RSLC system coupled to a Q Exactive Plus mass spectrometer (Thermo Fisher Scientific, Waltham, MA, USA) equipped with an EASY-spray ion source (Thermo Fisher Scientific). Peptides were washed on a trap column (PepMap100 C18, 0.3 x 5 mm, 5 μm, 100 Å, Thermo Fisher Scientific) and separated on an analytical column (PepMap RSLC C18, 75 μm x 50 cm, 2 μm, 100 Å, Thermo Fisher Scientific). Raw data were processed using the Sequest HT search engine contained in the Proteome Discoverer software, version 2.0 (Thermo Scientific). Peptide searches were performed against the human proteome (UniProt [https://www.uniprot.org/]) and internal common contaminants databases, supplemented with the AL59 sequence determined in this study. Matching the obtained peptides to the available λ–C_L sequences in the UniProt database, the AL59 C_L-domain was identified. Further detailed about the C- and N-termini labeling and N-glycosylation proteomic analyses were described previously [24,28]. In all database searches semi-tryptic peptides were considered. Glycans were evaluated indirectly by identifying peptides with deamidated asparagine, obtained by PNGase F digestion [24].

Electron microscopy (EM)

Negative stain. To evaluate the quality and concentration of amyloid, extracts were analysed by negative stain EM, as described previously [16]. Grids were imaged on a Talos L120C transmission electron microscope (Thermo Scientific) operating at 120 keV.

Single-particle cryo-EM sample preparation and data collection. Samples were mixed by vortexing for 10 s at room temperature. Droplets of 3 µl were incubated for 30 s on freshly glow-discharged holey thick carbon grids (C-flat 1.2/1.3 C, Protochips), and plunge-frozen in liquid ethane using a Vitrobot Mk IV (Thermo Fischer Scientific), operated at 4 °C and 100% humidity. The main dataset comprising 2,049 movies was collected automatically on a Talos Arctica 200kV (Thermo Fisher Scientific), equipped with a Falcon 3 direct electron detector operated in electron counting mode (Supplementary Tab. 2). Movies were recorded at a nominal magnification of 120,000, corresponding to a pixel size of 0.889 Å/pixel and a total dose of 40 $e^-/Å^2$, equally distributed over 40 fractions. A second dataset comprising 2,556 movies was collected on the same microscope operated with the same settings, except for a lower magnification of ×73,000 corresponding to a pixel size of 1.43 Å.

Helical reconstruction of AL59. The structure of AL59 was reconstructed following standard protocols in RELION 3.1 [44,45,74,75]. 1,366 dose-weighted, motion- and CTF-corrected micrographs were selected from the main dataset based on a CTF-fitting resolution cut-off set to ≤ 10 Å. 5,112 fibrils were picked start-to-end manually from the micrographs in RELION 3.1 [44,45,74,75]. A first set of 44,115 long segments was extracted with 1,800-pixel box-size, binned by 6, and an inter-box distance of 30 Å. The tube diameter was set to 150 Å. A single reference-free 2D class average was used for initial model generation following published protocols [44], by applying an estimated crossover distance of 1,200 Å (Supplementary Fig. 2a). Extraction of short segments with a 340 pixel box-size and inter-box distance of 30 Å yielded 121,553 segments. Reference-free 2D classes obtained with a regularization value of T = 8 yielded averages with clearly visible cross-β structure (Supplemental Fig. 2b). However, we note difficulties to match unambiguously the 2D classes to the two reconstructed structures (Supplementary Fig. 2b

and 2c): the first and second 2D class averages with narrow widths of ~80 Å could correspond to either the bent or straight structure. The third and fourth class may be assigned to the bent and straight structure, respectively, due to their different widths. The noticeable groove visible in the fifth and sixth class is observed only for the projected 2D class of the bent structure. The associated layer line profiles exhibited peaks at 4.9 Å (not shown). The initial model was re-scaled and re-windowed to match the un-binned short segments and low-pass-filtered to 10 Å. Initial 3D auto-refinement applying C1 symmetry as well as helical twist and rise values of -0.7° and 4.9 Å, respectively, yielded a 4.2 Å resolution map. 3D classification with a regularization value of T = 24 divided the segments into four classes with numbers of 56,257, 27,465, 21,793 and 16,038, which are referred to as blurry, mixed, straight and bent, respectively. Attempts to reconstruct the mixed class yielded a map with an estimated resolution of 5.2 Å after masking. The straight and bent classes were reconstructed separately by applying additional 3D refinement and classification rounds, reducing the segment numbers to 13,119 and 10,594 particles, respectively. Final 3D auto-refinement applying 5 Å low-pass filtered maps, 270 Å masks, helical tube radii of 135 Å and Z-values of 30%, yielded 4.0 and 4.1 Å resolution maps after masking for the straight and bent structures, respectively. Resolution values are based on the intersection of the half-map Fourier shell correlation applying the threshold at 0.143 (Supplementary Fig. 2d). The straight and bent maps were sharpened applying B-factors of -107 $Å^2$ and -101 $Å^2$, respectively.

Model building of AL59. The initial model of the straight structure was built *de novo* in Coot [76], starting from the position of the disulphide bond between Cys-22 and Cys-87. The polypeptide backbone of the model was extended by placement of poly-Alanine residues into the contiguous map. Considering bulky side-chain features, residues were

mutated to match the AL59 protein sequence. The model was iteratively built and refined in Coot, Chimera-Isolde and Phenix real-space refinement with reference-model restraints [76–79]. The additional density around Asn-19 was modelled as N-linked N-acetyl glucosamine (NAG), representing the first building block of the common N-glycan core [80]. The final model comprising five 120-residue long chains in each proto-filament was obtained by refinement with additional non-crystallographic symmetry (NCS) restraints. Phenix, Molprobity and EMDB validation [81–83] revealed map-model cross-correlation (CC_{mask}), EM-ringer and Molprobity-score values of 0.78, 5.3 and 1.6 (Supplementary Tab. 2). To model the bent structure, fragments of the straight structural model were fit into the map as rigid bodies in Coot [76]. The combined fragments were refined iteratively, as described for the straight structure. The final model of the bent structure comprises five chains, each encompassing residues 5-97 and 103-111, and exhibits map-model cross-correlation (CC_{mask}), EM-ringer and Molprobity-score values of 0.74, 3.2 and 2.2, respectively.

SPA of collagen VI. 1,768 particles were picked manually in the micrographs of the main dataset with a pixel size of 0.889 Å. The particles were extracted applying particle-box and diameter-background sizes of 1,126 and 844 pixels, respectively. To increase the number of particles, additional 1,004 particles were picked manually from the second dataset with a pixel size of 1.43 Å. These particles were extracted applying particle-box and diameter-background sizes of 700 and 525, respectively. To match box- and pixel-size, the larger box was scaled to match the smaller one. After import of the particles into cryoSPARC [84], the particle box was scaled to 384 pixels, yielding a pixel size of 2.607 Å. The reconstructed *ab initio* map was refined homogeneously to an estimated resolution of 18 Å (Supplementary Fig. 5a and 5b). After map and particle re-orientation in ChimeraX [78], the number of particles was doubled by symmetry expansion and the map was

subsequently refined locally to a resolution of 13 Å (Supplementary Fig. 5c). Enforced C2 symmetry during local refinement improved map resolution to 12 Å, but did not improve markedly map interpretability (Supplementary Fig. 5d). To estimate the available space of the quarter-bead volume, we placed 11 copies of an AI-model of α2-VWFA2 [https://www.uniprot.org/uniprotkb/P12110/entry]. The crystal structure of a collagen triple helix [https://www.rcsb.org/structure/1k6f] [60] was assembled into elongated parallel tetramers (Supplementary Fig. 6).

Cryo-EM SPA of the AL59/COLVI complex. In Relion [44,45,74,75], 36,540 helical segments with a tube diameter of 500 Å were extracted from the manually picked 5,112 fibrils, applying box-size and inter-box distance values of 840 and 84 pixels, respectively. The box was re-scaled to 280 pixels. Particles associated with their micrographs were imported into cryoSPARC [84] for 2D classification. Applying a maximum resolution of 10 Å, an initial classification uncertainty factor of 50, and a batch-size of 200 per class, the particles were sorted into 400 classes. Two classes comprising 119 particles were interpreted as amyloid with associated COLVI-bead. 37 particles with an inter-particle separation distance below 400 Å were removed as duplicates. 78 of the remaining 82 particles were aligned to yield the 2D class presented in Fig. 5d. To provide a visual guide, the reconstructed map of the COLVI-bead was arranged with a surface of the AL59 fibril to match the shape of the 2D class average in ChimeraX [78].

Immuno-electron microscopy (IEM). 10 µl drop of the AL59 extract were placed at room temperature for 30 minutes on a 200 mesh formvar/carbon coated nichel grid (EMS, Hatfield, PA, USA). After absorbing the excess of the suspension with Whatman filter paper, fibrils were then incubated with a rabbit anti-human collagen VI (1:10, Fitzgerald Industries International) overnight at 4°C in a wet chamber, followed by a donkey anti-rabbit antibody conjugated to a 12 nm colloidal gold (1:75, Jackson Immunoresearch) in

494 block solution for 45 minutes at 37°. After post-fixation with 2% glutaraldehyde, grids
495 were finally negatively counterstained with 2% uranyl acetate and observed with an
496 Energy Filter Transmission Electron Microscope (EFTEM, ZEISS LIBRA® 120)
497 equipped with YAG scintillator slow scan CCD camera (Sharp eye, TRS, Moorenweis,
498 Germany).

499 ***Cryogenic electron tomography (cryo-ET).*** Samples were prepared in the same way as
500 for SPA. Vitrified specimens were imaged on a Titan Krios cryo-transmission electron
501 microscope equipped with a Selectris energy filter with a slit width of 15 eV and a Falcon
502 IV direct electro detector (Thermo Fisher Scientific). Multiple tilt series with a pixel size
503 of 2.32 Å were recorded over a tilt range of -54 to 54 degrees in 3-degree steps with a
504 dose-symmetric scheme using SerialEM and PACE-tomo 1.2 [85,86]. The total electron dose
505 was kept under 120 electrons/Å². Frames were aligned using MotionCor2 1.5.0 [75]. Final
506 tilt series were aligned using fiducial-less patch tracking, down sampled four times, and
507 reconstructed into tomograms by back projection within IMOD 4.11.15 [87]. Contrast was
508 enhanced by filtering the tomograms using CTF Deconvolve of isonet 0.2 [88].

509 Tomograms were segmented using Amira (Thermo Fisher Scientific) as follows: amyloid
510 fibrils were detected using Amira's XTracing module based on cross-correlation with a
511 cylindrical template (5 nm in radius and 25 nm in length). Cross-correlation fields were
512 thresholded to balance the amount of true positives and negatives. Amyloid fibrils were
513 then traced using a search cone 15 nm in length and 10° angle, with a direction coefficient
514 of 0.3 and minimum fibril length of 25 nm. Decorating polymers as well as free COLVI
515 were segmented manually. Pixels with a grey-scale value close to that of the solvent were
516 filtered out using a threshold. Images of the three-dimensional rendering were produced
517 in ChimeraX [78]. To investigate whether amyloid-bound COLVI polymers adopted the
518 same or a different helical symmetry than the amyloid, a ball model was constructed with

519 helical twist and rise of AL59 but larger radius (60 Å) using SPIDER 26.06 [89]. For better
520 visualization, balls were displayed only every tenth AL59 subunit. Visual inspection
521 revealed an almost complete overlap between the COLVI density and the helical model.

522

523 **Data analysis, visualization and availability**

524 Structures and derived data were analyzed and visualized using Arpeggio and FATCAT
525 webservers as well as Rstudio, ChimeraX [78,90–93] and PyMol (Schrödinger, NY, USA). To
526 obtain the 3D class distribution among fibrils, metadata stored in the Relion STAR file
527 were analysed applying a custom-made R script. For the alignment of the AL amyloid
528 sequences shown in Fig. 4a, C_L sequences of λ1-FOR001 and λ1-FOR006, reported to
529 residue Ser-114 [18], were extended to Pro-119 based on aligned [43] precursor sequences
530 [https://www.ncbi.nlm.nih.gov/protein/S05270] and [https://www.ncbi.nlm.nih.gov
531 /protein/ANN81987.1?report=genpept], respectively. Sequences were aligned and
532 visualized using Uniprot, Blast, ClustalOmega and ESPript [94–97].

533 The reconstructions and models of the straight and bent AL59 amyloids were deposited in
534 the EMDB and PDB with the following accession codes: PDB: 8CDH and EMDB: EMD-
535 16573, and PDB: 8CDI and EMDB: EMD-16574, respectively. The raw cryo-EM images
536 used in our SPA analysis were deposited in EMPIAR under the accession code:
537 EMPIAR-11408. The COLVI map was deposited under EMD-18689.

Acknowledgements

This study was partially supported by Ricerca Corrente funding from Italian Ministry of Health to IRCCS Policlinico San Donato; Centro di Ricerca Pediatrica, Fondazione Romeo and Enrica Invernizzi (Milan, Italy); Italian Ministry of Research PRIN 2020 (20207XLJB2); Deutsche Forschungsgemeinschaft (DFG, German Research Foundation) under Germany's Excellence Strategy (EXC 2067/1-390729940) and Italian Ministry of Health (RF-2016-02361756). Cryo-ET instrumentation was jointly funded by the DFG Major Research Instrumentation program (448415290) and the Ministry of Science and Culture of the State of Lower Saxony. K.S. and R.F.-B. were funded by the joint efforts of The Michael J. Fox Foundation for Parkinson's Research (MJFF) and the Aligning Science Across Parkinson's (ASAP) initiative. MJFF administers the grant ASAP-000282 on behalf of ASAP and itself. We are grateful to T. Cheng for assistance in cryo-ET experiments and T. Shaikh for advice on cryo-ET data processing.

Author contributions

Conceptualization and Supervision by R.F.B., G.P., A.C.S., S.R. Investigation and Analysis by T.S., A.C.S., V.S., K.S., G.Maz., S.C., C.M., P.R., A.C., P.F., P.M. Funding acquisition and Resources by G.Mer., G.P., L.A., C.P., R.F.B., M.B., S.R. Original draft by T.S, V.S., G.Maz., K.S., A.C. Review and Editing by G.Mer., M.B., M.N, G.P., R.F.B., L.D., S.R. Data visualization by T.S., K.S, G.Maz, A.C., edited and reviewed by T.S. and S.R. Contribution to and approval of the submitted version by all authors.

Competing interests

The authors declare no competing interests.

Figures

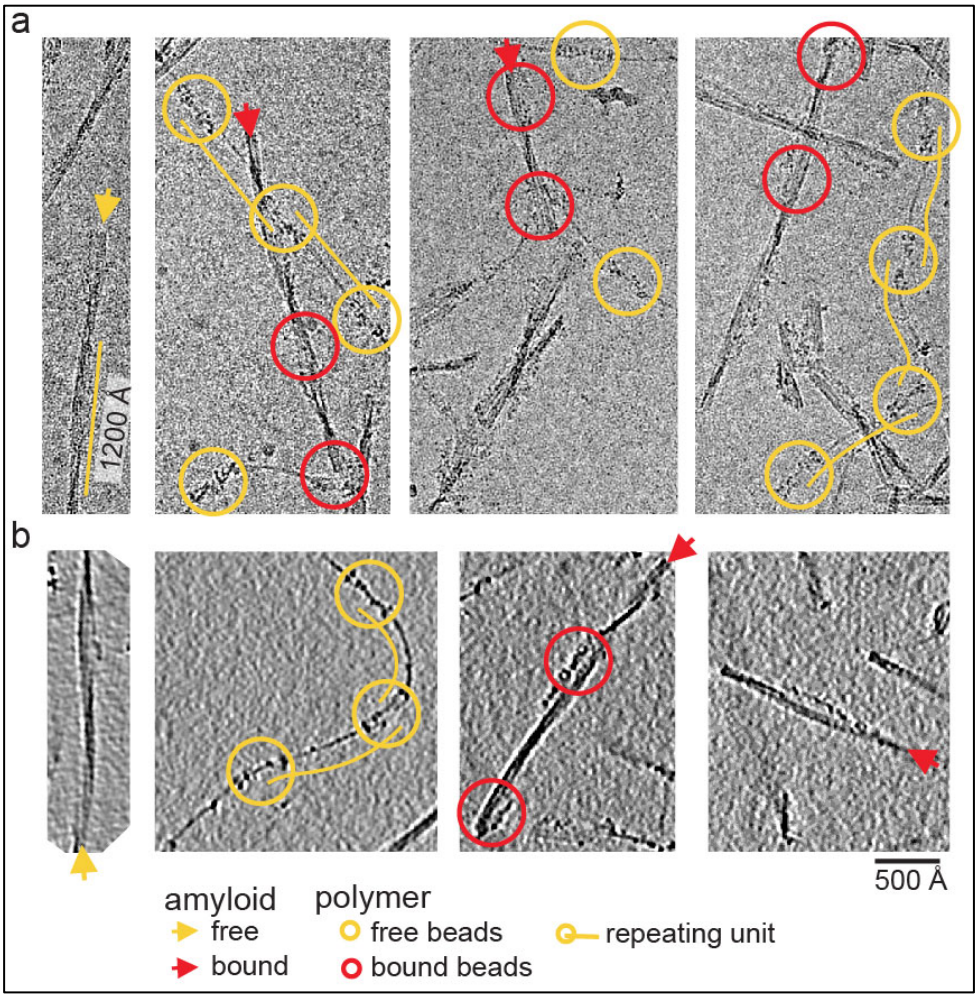

Figure 1. AL59 extract comprises additional polymer decorating the amyloid fibrils.

(a) Cryo-EM micrographs and (b) Cryo-ET 2D projections reveal undecorated and polymer-decorated AL59 fibrils, highlighted by yellow and red arrows, respectively. The remarkably shaped polymer beads are encircled in yellow and red for the unbound and amyloid-associated forms, respectively. A thin yellow line indicated the estimated crossover-length. The image scale-bar is valid for both panels. See Supplementary Fig. 2.

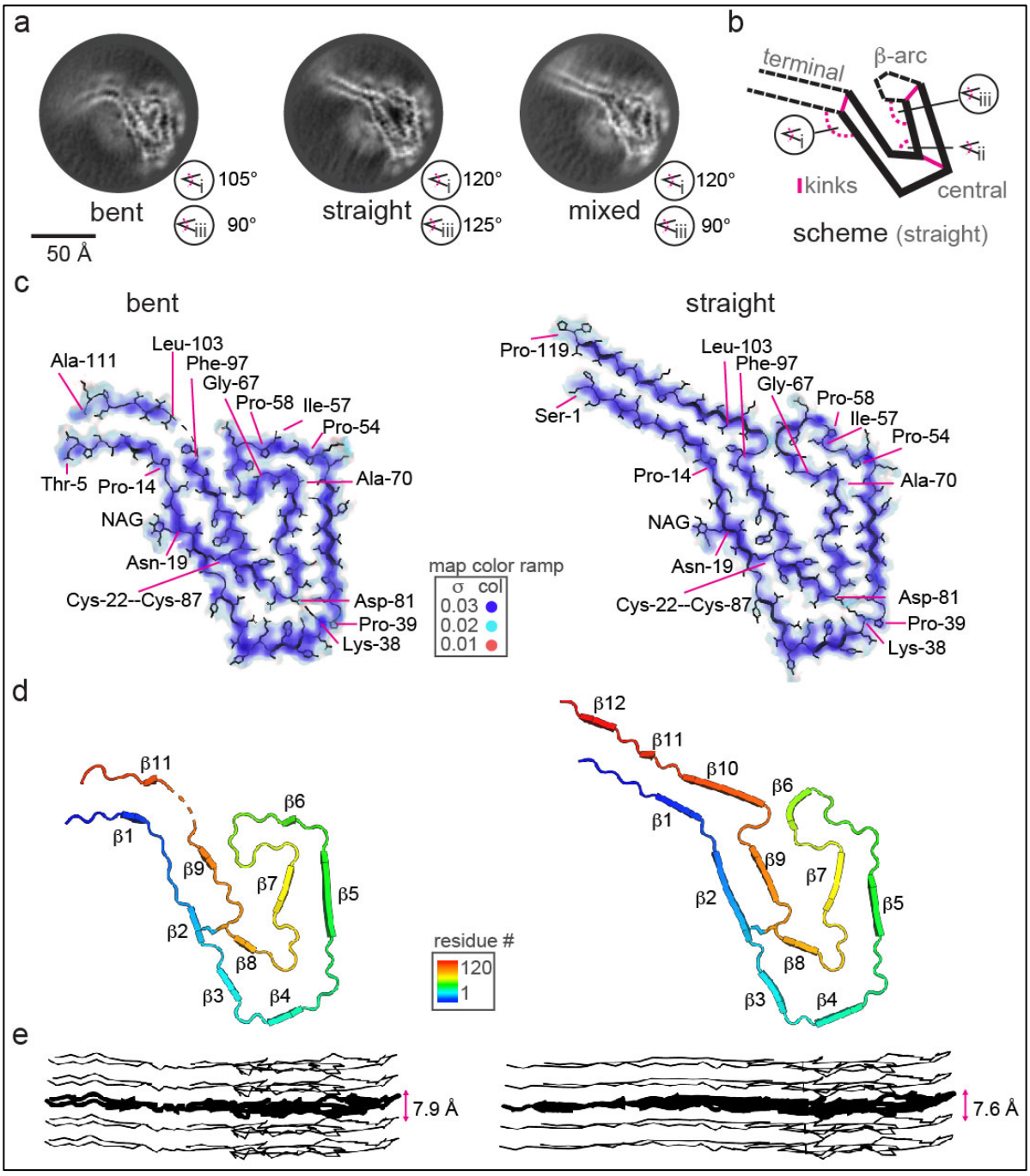

Figure 2. ***Structures of glycosylated AL59 display a stable central core and two flexible segments adopting alternative conformations***

(a) Standard helical processing yielded three distinct 3D class averages, shown as cross-sections on grey scale. (b) Structural variations of the shared fold are described based on the depicted scheme of the straight class. The stable centre, shared among all classes, is shown as straight black line. The terminal and β-arc segments with alternative conformations are drawn

as dotted black lines. The three kinks and angles are highlighted by straight and dotted pink lines, respectively. The kink angles with alternative conformations in the three classes are highlighted. (c) Cross-sectional views of reconstructed maps, visualized according to the depicted σ-colour scale. The polypeptide backbone and side-chains of the models are shown as black cartoon and sticks, respectively. (d) The polypeptide backbones are shown as cartoons, coloured on a rainbow-spectrum for residue numbers from 1 to 120. (e) Side-view of the deposited models comprising five subunits in each proto-filament. The height differences of the polypeptide layers are indicated for the central layer, highlighted as thick ribbon. See Supplementary Fig. 3.

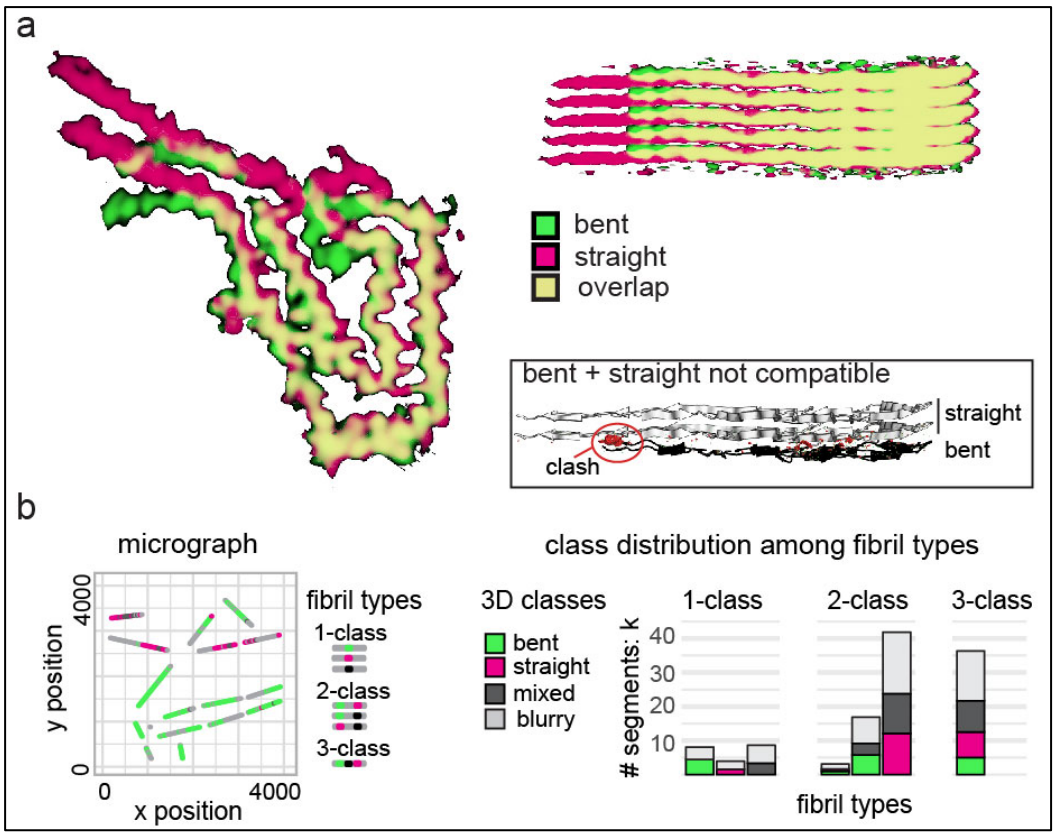

Figure 3. Alternative conformations of the terminal segments in the bent and straight structures are sterically incompatible and distributed on separate fibrils

(a) Cross-sectional and side-view of the superimposed maps of the bent and straight structures are shown in green and magenta, respectively. Matching segments appear yellow. *Inset*: adding a single layer of the bent structure to the end of a straight fibril leads to clashes of their terminal segments (highlighted in red). (b) *left:* Bent, straight and mixed class segments are coloured green, magenta and dark grey to visualize their distribution among 16 fibrils in a single representative micrograph. Segments without interpretable structure, labelled blurry, are shown in light grey. The analysis of the fibrils in all micrographs is shown on the *right*: fibrils comprising a single, two and three classes are denoted as 1-class, 2-class and 3-class fibrils, respectively. See Supplementary Fig. 4.

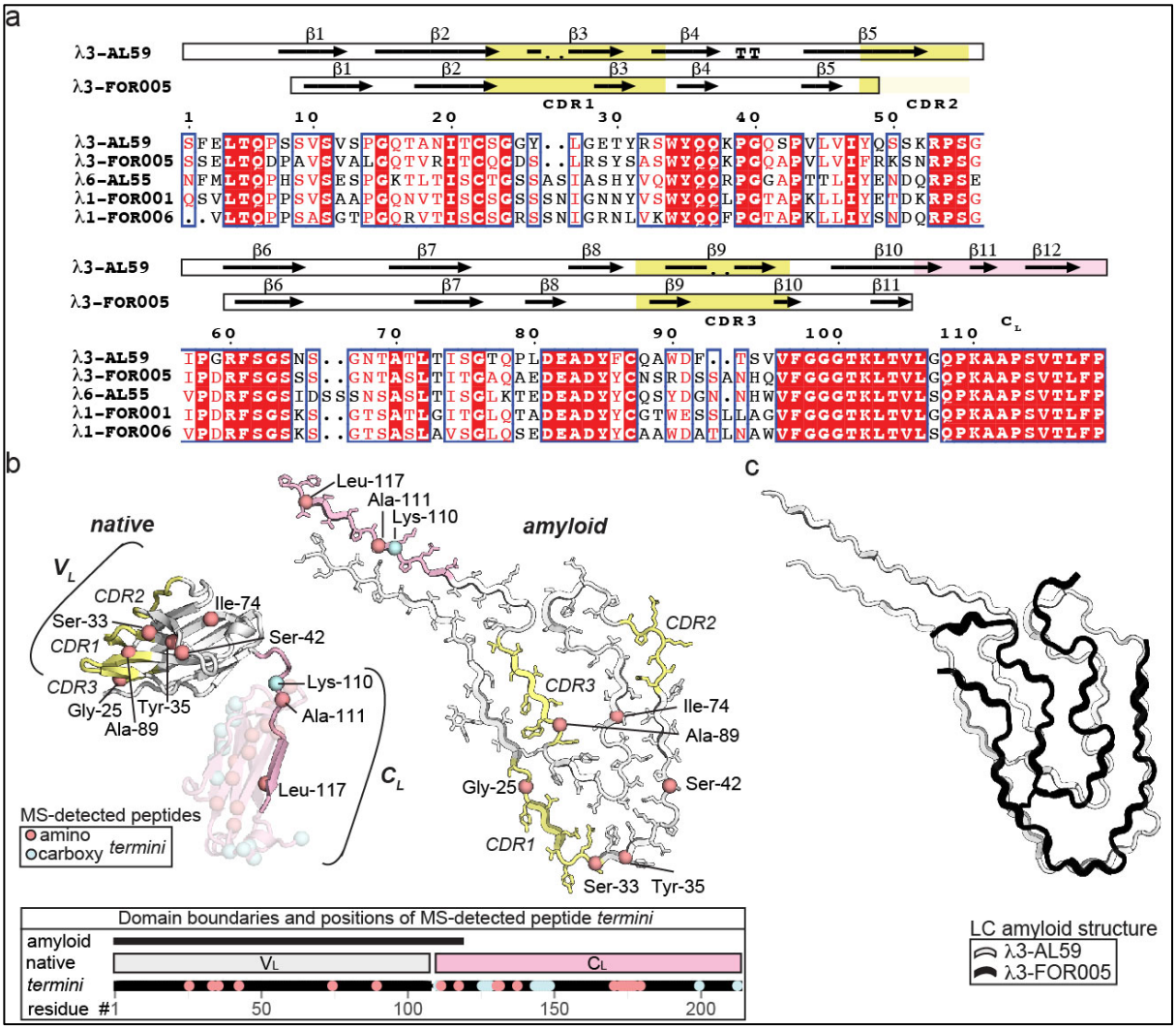

Figure 4. AL59 adopts a fold related to λ3-FOR005, but harbours an extended constant domain (C_L) fragment in its amyloid core

(a) Sequence alignment of AL59 belonging to the λ3 gene to the four other *ex vivo* LC amyloid structures [3,15–18], λ3-FOR005 [https://www.rcsb.org/structure/6Z1O], λ6-AL55 [https://www.rcsb.org/structure/6HUD], λ1-FOR001 [https://www.rcsb.org/structure/7NSL] and λ1-FOR006 [https://www.rcsb.org/structure/6IC3]. The alignment was visualized using ESPript [95]. β-strands and strict β-turns are indicated by numbered βand non-numbered TT symbols, respectively. Strict sequence identity is indicated by a red box with white character, similarities within and across groups are indicated by red characters and blue frames, respectively. Secondary structure elements of λ3-AL59 and λ3-FOR005 are shown above. CDR segments of λ3-AL59 and λ3-FOR005 are labelled and highlighted in yellow and orange, respectively. The C_L-derived fragment in the amyloid core of AL59 is highlighted in light pink. (b) The AI-generated native AL59 structure (*left*) is compared to the straight amyloid structure (*right*). V_L and C_L domains are coloured white and light pink, respectively. The CDRs are coloured yellow and labelled. The non-amyloidogenic C_L part is semi-transparent. Modified N- and C-*termini* of LC peptide fragments detected by LC-MS/MS are shown as red and blue Cα-spheres, respectively. The residue-level line-plot depicts the domain boundaries and modified N- and C-*termini* of LC fragments detected by LC-MS/MS. (c) The superimposed λ3-AL59 and λ3-FOR005 structures are shown as white and black cartoons, respectively.

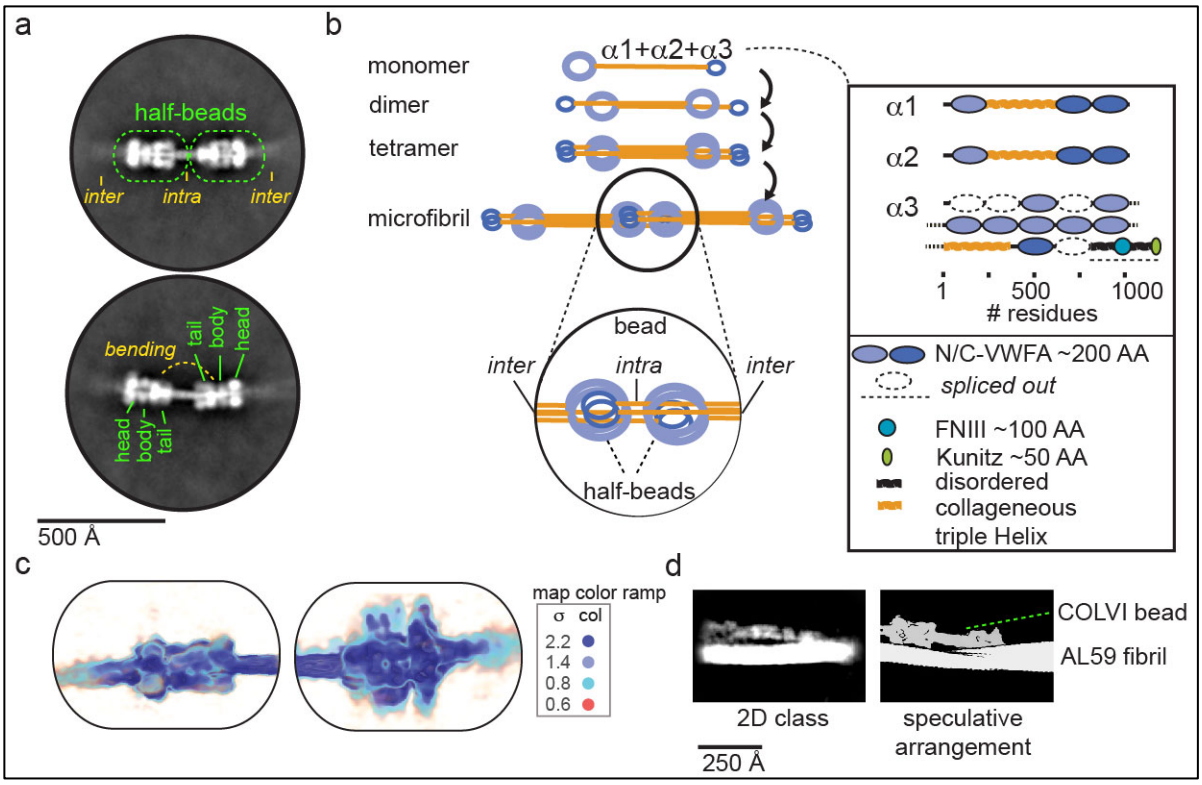

Figure 5. Collagen VI is the abundant polymer concatenating with AL59

(a) The two 2D class averages obtained for the manually picked beads reveal two half-beads linked by an intra-bead fibre. Inter-bead fibres are hardly visible, likely due to high flexibility. Each half-bead entails head, body and tail substructures, as indicated in pink for the second 2D class average. The angles of the two half-beads differ between the two classes, indicating flexible bending of the intra-bead fibre. (b) The Collagen VI assembly model [51,55] depicts that three subunits assemble hierarchically into bead-on-a-string microfibrils. (*right*) The monomeric building block is composed of subunits α1, α2 and α3. Each ~1k residue-long α1 and α2 subunit comprises a single N- and two C-terminal von Willebrand factor homologous domains (VWFA), separated by ~300 residue long collagen segments. The >3k residue-long α3 subunit comprises ten and two VWFA domains at its N- and C-*terminus*, respectively, separated by a ~300 residue long collagen region. Alternative splicing of α3 [55,98] reduces the number of N- and C-terminal VWFA domains to seven and one, respectively.

634 Microfibrils lack most likely the C-terminal type-III Fibronection (FNIII) and Kunitz
635 domains due to post-translational cleavage. (*left*) In the first step of microfibril formation, the
636 three subunits assemble parallel via their central collagen regions into the monomeric
637 building block. Dimers and tetramers assemble successively from anti-parallel and parallel
638 monomers and dimers, respectively. Finally, bead-on-a-string microfibrils arrange head-to-
639 head to tetramers [51,55]. (c) Two views of the half-bead map are oriented to match the upper
640 2D class average shown in panel a. The map volume is visualized according to depicted σ-
641 colour scale. The main features (darker blue) are comparable to a map at a threshold of 1.5 σ.
642 (d) *Left*: the reference-free 2D class average, obtained by single-particle processing of helical
643 segments, features a bright tube decorated by a darker shape resembling the COLVI-bead.
644 *Right*: the reconstructed map of the COLVI-bead was arranged with a surface of the AL59
645 fibril to match the shape of the 2D class average. The speculative arrangement was created as
646 visual guide. See Supplementary Fig. 5 and 6.

647

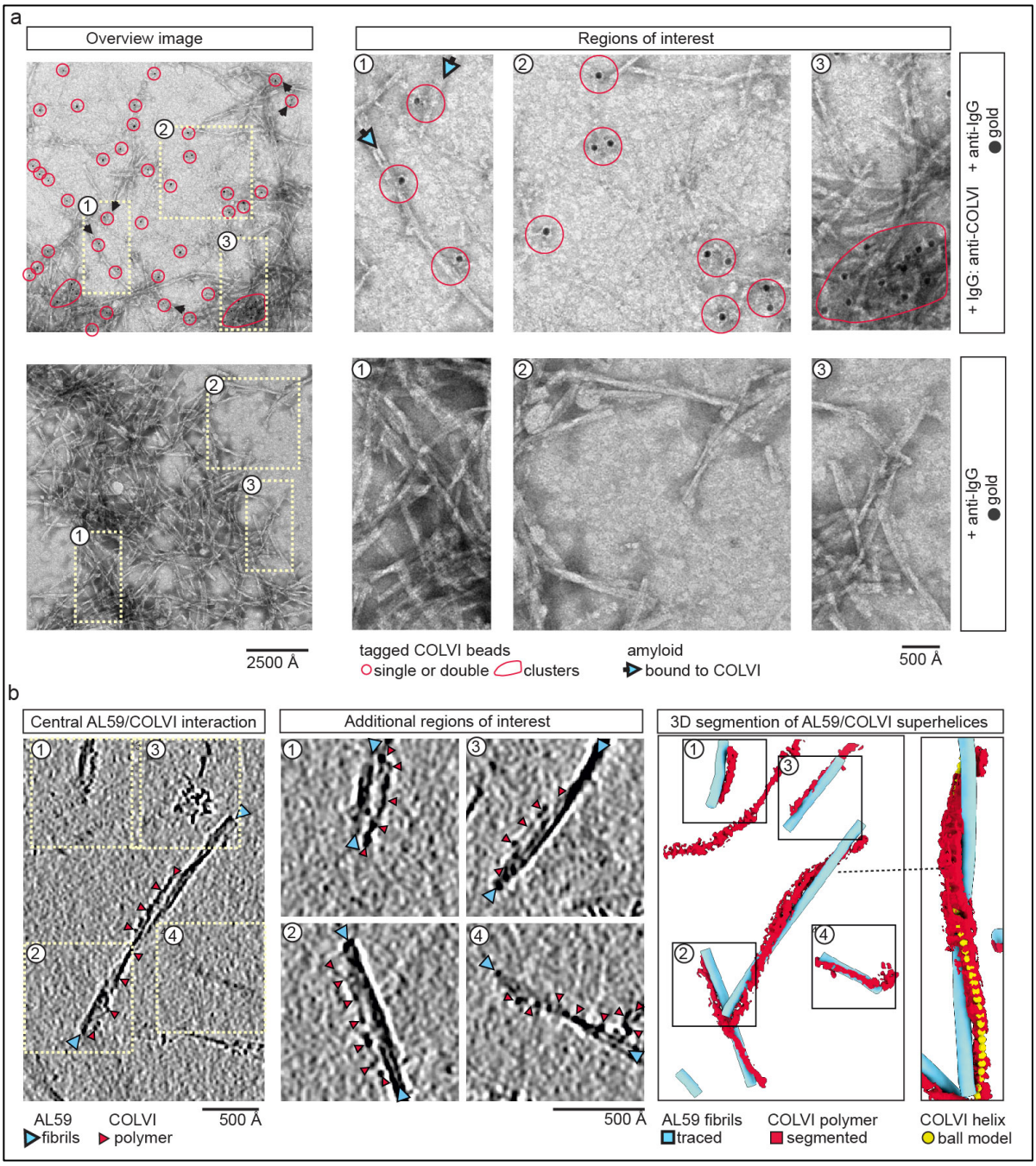

Figure 6. The fibril-decorating polymer is COLVI and follows the helical pitch of AL59

(a) Immuno-electron microscopy (IEM) revealed AL59 fibrils, free polymer and dense fibril clusters tagged with gold particles. *Top panel*: > 50 gold particles, highlighted in red, were counted in this image of the extract stained with anti-COLVI IgG and gold-conjugated anti-IgG antibodies 70R-CR009x (Fitzgerald) [61] followed by a 12 nm gold-conjugated anti-IgG antibody. respectively. Three magnified sections emphasize (1) three gold particles within

~150 Å distance to AL59 fibrils, (2) three single gold particles and three duplets tagging free COLVI polymer as well as (3) 11 gold particles within a dense amyloid fibril cluster. *bottom panel*: No gold particles were found in the sample treated only with the gold-conjugated anti-IgG antibodies. Three magnified sections are shown for direct comparison to the top panel. See Supplementary Fig. 7 and 8.

(b) *Left:* An overview cryo-ET slice with a thickness of 0.925 nm and four additional regions of interest (highlighted boxes) reveal amyloid fibrils (blue arrowheads) decorated with COLVI polymers (green arrowheads). The height level of the overview slice highlights the central AL59/COLVI interaction. The four boxes are shown at different height levels and higher magnification. *Right*: 3D renderings of the overview cryo-ET slice and the highlighted central AL59/COLVI interaction show traced AL59 fibril tubes (blue) decorated with segmented COLVI densities (green). A helical ball model (yellow) with helical twist and rise of AL59, but three times larger helical radius, is shown within the COLVI density to demonstrate the helical imprinting of AL59 on COLVI.

References

1. Merlini, G. *et al.* Systemic immunoglobulin light chain amyloidosis. *Nat. Rev. Dis. Primer* **4**, 1–19 (2018).
2. Merlini, G. AL amyloidosis: from molecular mechanisms to targeted therapies. *Hematol. Am. Soc. Hematol. Educ. Program* **2017**, 1–12 (2017).
3. Haupt, C. The AL Amyloid Fibril: Looking for a Link between Fibril Formation and Structure. *Hemato* **2**, 505–514 (2021).
4. Del Pozo-Yauner, L. *et al.* Role of the mechanisms for antibody repertoire diversification in monoclonal light chain deposition disorders: when a friend becomes foe. *Front. Immunol.* **14**, (2023).
5. Bodi, K. *et al.* AL-Base: a visual platform analysis tool for the study of amyloidogenic immunoglobulin light chain sequences. *Amyloid* **16**, 1–8 (2009).
6. Perfetti, V. *et al.* The repertoire of λ light chains causing predominant amyloid heart involvement and identification of a preferentially involved germline gene, IGLV1-44. *Blood* **119**, 144–150 (2012).
7. Prokaeva, T. *et al.* Soft tissue, joint, and bone manifestations of AL amyloidosis: Clinical presentation, molecular features, and survival. *Arthritis Rheum.* **56**, 3858–3868 (2007).
8. Abraham, R. S. *et al.* Immunoglobulin light chain variable (V) region genes influence clinical presentation and outcome in light chain–associated amyloidosis (AL). *Blood* **101**, 3801–3807 (2003).
9. Merlini, G. & Palladini, G. Light chain amyloidosis: the heart of the problem. *Haematologica* **98**, 1492–1495 (2013).
10. Absmeier, R. M., Rottenaicher, G. J., Svilenov, H. L., Kazman, P. & Buchner, J. Antibodies gone bad – the molecular mechanism of light chain amyloidosis. *FEBS J.* **290**, 1398–1419 (2023).

11. Oberti, L. *et al.* Concurrent structural and biophysical traits link with immunoglobulin light chains amyloid propensity. *Sci. Rep.* **7**, 16809 (2017).
12. Bourne, P. C. *et al.* Three-dimensional structure of an immunoglobulin light-chain dimer with amyloidogenic properties. *Acta Crystallogr. D Biol. Crystallogr.* **58**, 815–823 (2002).
13. Schiffer, M., Girling, R. L., Ely, K. R. & Edmundson, A. B. Structure of a λ-type Bence-Jones protein at 3.5-Å resolution. *Biochemistry* **12**, 4620–4631 (1973).
14. Graziani, M. S. & Merlini, G. Serum free light chain analysis in the diagnosis and management of multiple myeloma and related conditions. *Expert Rev. Mol. Diagn.* **14**, 55–66 (2014).
15. Radamaker, L. *et al.* Cryo-EM reveals structural breaks in a patient-derived amyloid fibril from systemic AL amyloidosis. *Nat. Commun.* **12**, 875 (2021).
16. Swuec, P. *et al.* Cryo-EM structure of cardiac amyloid fibrils from an immunoglobulin light chain AL amyloidosis patient. *Nat. Commun.* **10**, 1269 (2019).
17. Radamaker, L. *et al.* Cryo-EM structure of a light chain-derived amyloid fibril from a patient with systemic AL amyloidosis. *Nat. Commun.* **10**, 1103 (2019).
18. Radamaker, L. *et al.* Role of mutations and post-translational modifications in systemic AL amyloidosis studied by cryo-EM. *Nat. Commun.* **12**, 6434 (2021).
19. Puri, S. *et al.* The Cryo-EM STRUCTURE of Renal Amyloid Fibril Suggests Structurally Homogeneous Multiorgan Aggregation in AL Amyloidosis. *J. Mol. Biol.* **435**, 168215 (2023).
20. Shi, Y. *et al.* Structure-based classification of tauopathies. *Nature* **598**, 359–363 (2021).
21. Yang, Y. *et al.* Cryo-EM structures of amyloid-β 42 filaments from human brains. *Science* **375**, 167–172 (2022).
22. Kumar, S. *et al.* Assay to rapidly screen for immunoglobulin light chain glycosylation: a potential path to earlier AL diagnosis for a subset of patients. *Leukemia* **33**, 254–257 (2019).
23. Mellors, P. W. *et al.* MASS-FIX for the detection of monoclonal proteins and light chain N-glycosylation in routine clinical practice: a cross-sectional study of 6315 patients. *Blood Cancer J.* **11**, 50 (2021).

24. Nevone, A. *et al.* An N-glycosylation hotspot in immunoglobulin κ light chains is associated with AL amyloidosis. *Leukemia* **36**, 2076–2085 (2022).
25. Kourelis, T. *et al.* MASS-FIX may allow identification of patients at risk for light chain amyloidosis before the onset of symptoms. *Am. J. Hematol.* **93**, E368–E370 (2018).
26. Buxbaum, J. N. *et al.* Amyloid nomenclature 2022: update, novel proteins, and recommendations by the International Society of Amyloidosis (ISA) Nomenclature Committee. *Amyloid* **29**, 213–219 (2022).
27. Gottwald, J. & Röcken, C. The amyloid proteome: a systematic review and proposal of a protein classification system. *Crit. Rev. Biochem. Mol. Biol.* **56**, 526–542 (2021).
28. Lavatelli, F. *et al.* Mass spectrometry characterization of light chain fragmentation sites in cardiac AL amyloidosis: insights into the timing of proteolysis. *J. Biol. Chem.* **295**, 16572–16584 (2020).
29. Lavatelli, F. *et al.* Amyloidogenic and associated proteins in systemic amyloidosis proteome of adipose tissue. *Mol. Cell. Proteomics MCP* **7**, 1570–1583 (2008).
30. Vrana, J. A. *et al.* Classification of amyloidosis by laser microdissection and mass spectrometry-based proteomic analysis in clinical biopsy specimens. *Blood* **114**, 4957–4959 (2009).
31. Rømer, A. M. A., Thorseth, M.-L. & Madsen, D. H. Immune Modulatory Properties of Collagen in Cancer. *Front. Immunol.* **12**, 791453 (2021).
32. Bonnans, C., Chou, J. & Werb, Z. Remodelling the extracellular matrix in development and disease. *Nat. Rev. Mol. Cell Biol.* **15**, 786–801 (2014).
33. Hynes, R. O. The extracellular matrix: not just pretty fibrils. *Science* **326**, 1216–1219 (2009).
34. Richey, T. *et al.* Macrophage-Mediated Phagocytosis and Dissolution of Amyloid-Like Fibrils in Mice, Monitored by Optical Imaging. *Am. J. Pathol.* **189**, 989–998 (2019).
35. Jackson, J. W. *et al.* Collagen inhibits phagocytosis of amyloid in vitro and in vivo and may act as a 'don't eat me' signal. *Amyloid* **0**, 1–12 (2022).

36. Giorgetti, S. *et al.* β2-Microglobulin isoforms display an heterogeneous affinity for type I collagen. *Protein Sci.* **14**, 696–702 (2005).
37. Homma, N., Gejyo, F., Isemura, M. & Arakawa, M. Collagen-binding affinity of beta-2-microglobulin, a preprotein of hemodialysis-associated amyloidosis. *Nephron* **53**, 37–40 (1989).
38. Hoop, C. L. *et al.* Collagen I Weakly Interacts with the β-Sheets of β2-Microglobulin and Enhances Conformational Exchange To Induce Amyloid Formation. *J. Am. Chem. Soc.* **142**, 1321–1331 (2020).
39. Relini, A. *et al.* Collagen Plays an Active Role in the Aggregation of β2-Microglobulin under Physiopathological Conditions of Dialysis-related Amyloidosis*. *J. Biol. Chem.* **281**, 16521–16529 (2006).
40. Kalaria, R. N. & Pax, A. B. Increased collagen content of cerebral microvessels in Alzheimer's disease. *Brain Res.* **705**, 349–352 (1995).
41. Shi, C., Gottschalk, W. K., Colton, C. A., Mukherjee, S. & Lutz, M. W. Alzheimer's Disease Protein Relevance Analysis Using Human and Mouse Model Proteomics Data. *Front. Syst. Biol.* **3**, 1085577 (2023).
42. Cheng, J. S. *et al.* Collagen VI protects neurons against Aβ toxicity. *Nat. Neurosci.* **12**, 119–121 (2009).
43. Mazzini, G. *et al.* Protease-sensitive regions in amyloid light chains: what a common pattern of fragmentation across organs suggests about aggregation. *FEBS J.* **289**, 494–506 (2022).
44. Scheres, S. H. W. Amyloid structure determination in RELION-3.1. *Acta Crystallogr. Sect. Struct. Biol.* **76**, 94–101 (2020).
45. He, S. & Scheres, S. H. W. Helical reconstruction in RELION. *J. Struct. Biol.* **198**, 163–176 (2017).
46. Dispenzieri, A. *et al.* N-Glycosylation of monoclonal light chains on routine MASS-FIX testing is a risk factor for MGUS progression. *Leukemia* **34**, 2749–2753 (2020).

47. Rottenaicher, G. J., Absmeier, R. M., Meier, L., Zacharias, M. & Buchner, J. A constant domain mutation in a patient-derived antibody light chain reveals principles of AL amyloidosis. *Commun. Biol.* **6**, 1–11 (2023).
48. Morgan, G. J. & Kelly, J. W. The Kinetic Stability of a Full-Length Antibody Light Chain Dimer Determines whether Endoproteolysis Can Release Amyloidogenic Variable Domains. *J. Mol. Biol.* **428**, 4280–4297 (2016).
49. Engvall, E., Hessle, H. & Klier, G. Molecular assembly, secretion, and matrix deposition of type VI collagen. *J. Cell Biol.* **102**, 703–710 (1986).
50. Furthmayr, H., Wiedemann, H., Timpl, R., Odermatt, E. & Engel, J. Electron-microscopical approach to a structural model of intima collagen. *Biochem. J.* **211**, 303–311 (1983).
51. Godwin, A. R. F., Starborg, T., Sherratt, M. J., Roseman, A. M. & Baldock, C. Defining the hierarchical organisation of collagen VI microfibrils at nanometre to micrometre length scales. *Acta Biomater.* **52**, 21–32 (2017).
52. Knupp, C. & Squire, J. M. A new twist in the collagen story—the type VI segmented supercoil. *EMBO J.* **20**, 372–376 (2001).
53. Baldock, C., Sherratt, M. J., Shuttleworth, C. A. & Kielty, C. M. The Supramolecular Organization of Collagen VI Microfibrils. *J. Mol. Biol.* **330**, 297–307 (2003).
54. Mouw, J. K., Ou, G. & Weaver, V. M. Extracellular matrix assembly: a multiscale deconstruction. *Nat. Rev. Mol. Cell Biol.* **15**, 771–785 (2014).
55. Beecher, N. *et al.* Collagen VI, Conformation of A-domain Arrays and Microfibril Architecture. *J. Biol. Chem.* **286**, 40266–40275 (2011).
56. Engel, J. *et al.* Structure and Macromolecular Organization of Type VI Collagena. *Ann. N. Y. Acad. Sci.* **460**, 25–37 (1985).
57. Shoulders, M. D. & Raines, R. T. Collagen structure and stability. *Annu. Rev. Biochem.* **78**, 929–958 (2009).

58. Bozec, L., van der Heijden, G. & Horton, M. Collagen Fibrils: Nanoscale Ropes. *Biophys. J.* **92**, 70–75 (2007).
59. Bella, J., Eaton, M., Brodsky, B. & Berman, H. M. Crystal and Molecular Structure of a Collagen-Like Peptide at 1.9 Å Resolution. *Science* **266**, 75–81 (1994).
60. Berisio, R., Vitagliano, L., Mazzarella, L. & Zagari, A. Crystal structure of the collagen triple helix model [(Pro-Pro-Gly)10]3. *Protein Sci. Publ. Protein Soc.* **11**, 262–270 (2002).
61. Endicott, J., Holden, P. & Fitzgerald, J. Authentication of collagen VI antibodies. *BMC Res. Notes* **10**, 358 (2017).
62. Morrow, S. M., Bissette, A. J. & Fletcher, S. P. Transmission of chirality through space and across length scales. *Nat. Nanotechnol.* **12**, 410–419 (2017).
63. G. Bäcklund, F. *et al.* Conducting microhelices from self-assembly of protein fibrils. *Soft Matter* **13**, 4412–4417 (2017).
64. McDermott, M. L., Vanselous, H., Corcelli, S. A. & Petersen, P. B. DNA's Chiral Spine of Hydration. *ACS Cent. Sci.* **3**, 708–714 (2017).
65. Kawauchi, T. *et al.* Encapsulation of Fullerenes in a Helical PMMA Cavity Leading to a Robust Processable Complex with a Macromolecular Helicity Memory. *Angew. Chem. Int. Ed.* **47**, 515–519 (2008).
66. Thomas, A. R. *et al.* Protein fibril assisted chiral assembly of gold nanorods. *J. Mater. Chem. B* **10**, 6360–6371 (2022).
67. Mankar, S., Anoop, A., Sen, S. & Maji, S. K. Nanomaterials: amyloids reflect their brighter side. *Nano Rev.* **2**, 10.3402/nano.v2i0.6032 (2011).
68. Misumi, Y. *et al.* Interaction between amyloid fibril formation and extracellular matrix in the proceedings of VIIIth International Symposium on Familial Amyloidotic Polyneuropathy. *Amyloid* **19**, 8–10 (2012).
69. Koike, H. & Katsuno, M. Transthyretin Amyloidosis: Update on the Clinical Spectrum, Pathogenesis, and Disease-Modifying Therapies. *Neurol. Ther.* **9**, 317–333 (2020).

70. Simpson, L. W., Szeto, G. L., Boukari, H., Good, T. A. & Leach, J. B. Collagen hydrogel confinement of Amyloid-β (Aβ) accelerates aggregation and reduces cytotoxic effects. *Acta Biomater.* **112**, 164–173 (2020).
71. Fernández de Larrea, C. *et al.* A practical approach to the diagnosis of systemic amyloidoses. *Blood* **125**, 2239–2244 (2015).
72. Gertz, M. A. *et al.* Definition of organ involvement and treatment response in immunoglobulin light chain amyloidosis (AL): A consensus opinion from the 10th International Symposium on Amyloid and Amyloidosis. *Am. J. Hematol.* **79**, 319–328 (2005).
73. Perfetti, V. *et al.* Inverse polymerase chain reaction for cloning complete human immunoglobulin variable regions and leaders conserving the original sequence. *Anal. Biochem.* **239**, 107–109 (1996).
74. Rohou, A. & Grigorieff, N. CTFFIND4: Fast and accurate defocus estimation from electron micrographs. *J. Struct. Biol.* **192**, 216–221 (2015).
75. Zheng, S. Q. *et al.* MotionCor2: anisotropic correction of beam-induced motion for improved cryo-electron microscopy. *Nat. Methods* **14**, 331–332 (2017).
76. Emsley, P. & Cowtan, K. Coot: model-building tools for molecular graphics. *Acta Crystallogr. D Biol. Crystallogr.* **60**, 2126–2132 (2004).
77. Croll, T. I. ISOLDE: a physically realistic environment for model building into low-resolution electron-density maps. *Acta Crystallogr. Sect. Struct. Biol.* **74**, 519–530 (2018).
78. Pettersen, E. F. *et al.* UCSF ChimeraX: Structure visualization for researchers, educators, and developers. *Protein Sci. Publ. Protein Soc.* **30**, 70–82 (2021).
79. Afonine, P. V. *et al.* Real-space refinement in PHENIX for cryo-EM and crystallography. *Acta Crystallogr. Sect. Struct. Biol.* **74**, 531–544 (2018).
80. Reily, C., Stewart, T. J., Renfrow, M. B. & Novak, J. Glycosylation in health and disease. *Nat. Rev. Nephrol.* **15**, 346–366 (2019).

81. Lawson, C. L. *et al.* EMDataBank unified data resource for 3DEM. *Nucleic Acids Res.* **44**, D396-403 (2016).
82. Afonine, P. V. *et al.* New tools for the analysis and validation of cryo-EM maps and atomic models. *Acta Crystallogr. Sect. Struct. Biol.* **74**, 814–840 (2018).
83. Davis, I. W. *et al.* MolProbity: all-atom contacts and structure validation for proteins and nucleic acids. *Nucleic Acids Res.* **35**, W375-383 (2007).
84. Punjani, A., Rubinstein, J. L., Fleet, D. J. & Brubaker, M. A. cryoSPARC: algorithms for rapid unsupervised cryo-EM structure determination. *Nat. Methods* **14**, 290–296 (2017).
85. Mastronarde, D. N. Automated electron microscope tomography using robust prediction of specimen movements. *J. Struct. Biol.* **152**, 36–51 (2005).
86. Eisenstein, F. *et al.* Parallel cryo electron tomography on in situ lamellae. *Nat. Methods* **20**, 131–138 (2023).
87. Kremer, J. R., Mastronarde, D. N. & McIntosh, J. R. Computer Visualization of Three-Dimensional Image Data Using IMOD. *J. Struct. Biol.* **116**, 71–76 (1996).
88. Liu, Y.-T. *et al.* Isotropic reconstruction for electron tomography with deep learning. *Nat. Commun.* **13**, 6482 (2022).
89. Frank, J. *et al.* SPIDER and WEB: processing and visualization of images in 3D electron microscopy and related fields. *J. Struct. Biol.* **116**, 190–199 (1996).
90. Wickham, H. *ggplot2: Elegant Graphics for Data Analysis*. (Springer International Publishing, 2016).
91. Wickham, H. *et al.* Welcome to the Tidyverse. *J. Open Source Softw.* **4**, 1686 (2019).
92. R Core Team. R: A language and environment for statistical computing. (2020).
93. Li, Z., Jaroszewski, L., Iyer, M., Sedova, M. & Godzik, A. FATCAT 2.0: towards a better understanding of the structural diversity of proteins. *Nucleic Acids Res.* **48**, W60–W64 (2020).
94. The UniProt Consortium. UniProt: the universal protein knowledgebase in 2021. *Nucleic Acids Res.* **49**, D480–D489 (2021).

95. Gouet, P., Courcelle, E., Stuart, D. I. & Métoz, F. ESPript: analysis of multiple sequence alignments in PostScript. *Bioinforma. Oxf. Engl.* **15**, 305–8 (1999).

96. Madden, T. L., Tatusov, R. L. & Zhang, J. Applications of network BLAST server. *Methods Enzymol.* **266**, 131–141 (1996).

97. Chenna, R. *et al.* Multiple sequence alignment with the Clustal series of programs. *Nucleic Acids Res.* **31**, 3497–500 (2003).

98. Dziadek, M. *et al.* Alternative splicing of transcripts for the alpha3 chain of mouse collagen VI: identification of an abundant isoform lacking domains N7–N10 in mouse and human. *Matrix Biol.* **21**, 227–241 (2002).

Supplementary Files

This is a list of supplementary files associated with this preprint. Click to download.

- 20231107AL59supplementfinal.pdf